

Low Temperature and Rapid Synthesis of Li-Rich $\text{Li}(\text{Li}_{0.17}\text{Mn}_{0.83})_2\text{O}_4$ Spinel Cathodes Derived from Metal-Organic Frameworks for Lithium-Ion Batteries

Ang Li,^[a, c] Ziqi Wang,^[a, c] Meihui Yu,^[b] and Ze Chang^{*[b]}

Li-rich spinel materials ($\text{Li}_{1+x}\text{Mn}_{2-x}\text{O}_4$) have shown promise for lithium-ion batteries. Nevertheless, the preparation of $\text{Li}_{1+x}\text{Mn}_{2-x}\text{O}_4$ faces significant challenges due to the difficulty in achieving a balance between well-crystallized phases and stoichiometric chemistry. Moreover, the synthesis process is highly sensitive to calcination temperature and time, making it susceptible to phase transformations. Therefore, the rational selection of precursors and corresponding calcination proce-

dures is absolutely essential. Herein, we make full use of the nature of metal-organic frameworks (MOFs) to achieve phase-controlled synthesis of $\text{Li}(\text{Li}_{0.17}\text{Mn}_{0.83})_2\text{O}_4$ (LMO-F) spinel cathodes in 8 minutes at 500 °C. The composition and structural evolution during the pyrolysis process were systematically investigated to clarify the relationship between precursors and derivatives. Notably, the LMO-F achieved good electrochemical performance with 100.4 mAh g⁻¹ at 50 mA g⁻¹ after 100 cycles.

Introduction

Lithium-ion batteries (LIBs) have been widely used in various portable electronic devices and energy vehicles.^[1] Currently, the cathode material remains the primary determinant of the total output capacity of LIBs.^[2] Among cathode materials, spinel lithium manganate (LiMn_2O_4) is a highly promising material due to its high voltage platform, low price and environmental friendliness.^[3] Nevertheless, the electrochemical performance of LiMn_2O_4 cathodes is hindered by the Jahn-Teller distortion of Mn³⁺, leading to significantly decreased cycle life.^[4] Designing and preparing of Li-rich spinel cathodes ($\text{Li}_{1+x}\text{Mn}_{2-x}\text{O}_4$) with Li⁺ partially substitution for Mn³⁺ is an effective strategy to promote the average oxidation state of Mn higher than 3.5+ or even achieve a compound with all Mn at 4+.^[5] However, the synthesis of $\text{Li}_{1+x}\text{Mn}_{2-x}\text{O}_4$ faces great challenges because it is difficult to establish a balance between the well-crystallized phase and stoichiometric chemistry.

In general, this type of material is synthesized through a heterogeneous solid-state reaction. It involves mixing lithium compounds (Li_2CO_3 , LiNO_3 , LiOH) with the manganese compounds (MnO_2 , Mn_3O_4 , $\text{Mn}(\text{NO}_3)_2$, MnCO_3) in a certain proportion, followed by calcination at high temperatures.^[6] High temperatures are used to promote cation diffusion into the

network of the precursors, although long time calcination is required, as this diffusion process is kinetically slow.^[6] Apparently, this procedure is time-consuming and energy-intensive, leading to low production efficiency and high costs. More importantly, the preparation process of stoichiometric $\text{Li}_{1+x}\text{Mn}_{2-x}\text{O}_4$ is sensitive to calcination temperature and time and is prone to phase transformations.^[4a] Therefore, the rational selection of precursors and corresponding calcination procedures is absolutely essential.

It is widely acknowledged that the interatomic distance of metal ions plays a pivotal role in the ion diffusion process, which in turn significantly impacts the formation of transition metal oxides during the thermal decomposition of precursors.^[7] Therefore, shortening the distance between Li ions and Mn ions is significant to low temperature and rapid preparation of Li-rich spinel materials. Metal-organic framework materials (MOFs) are a new class of crystalline porous materials, which are composed of metal ions and organic ligands combined through coordination bonds, with the characteristics of adjustable pores, large specific surface area and diverse composition, and have shown great potential in the field of energy.^[8] Actually, MOFs as homogeneous precursors are favorable for the synthesis of transition metal oxide cathodes because of the distance between the alkali and transition metals in the MOFs at the microscopic level.^[9] At the same time, MOFs possess a clear crystal structure, which is convenient for studying their composition and structural evolution during pyrolysis to establish a balance between the well-crystallized phase and stoichiometric chemistry of $\text{Li}_{1+x}\text{Mn}_{2-x}\text{O}_4$.

Herein, a low temperature and rapid synthesis strategy is developed for preparing Li-rich spinel $\text{Li}(\text{Li}_{0.17}\text{Mn}_{0.83})_2\text{O}_4$ cathode derived from $\text{LiMn}(\text{HCOO})_3$ (LiMn-MOF) precursor (Figure 1). The atomic-level homogenous distributions of Li ions and Mn ions in MOF promises a short migration distance of metal ions, enabling a fast phase formation of $\text{Li}(\text{Li}_{0.17}\text{Mn}_{0.83})_2\text{O}_4$ (LMO-F) in minutes. The phase transformation process from LiMn-MOF to

[a] A. Li, Z. Wang
School of Sciences, Civil Aviation University of China, Tianjin 300300, Jinbei Road 2898, Dongli District, Tianjin, P.R. China

[b] M. Yu, Z. Chang
School of Materials Science and Engineering, Nankai University, Tianjin 300350, Tongyan Road 38, Jinnan District, Tianjin, P.R. China
E-mail: changze@nankai.edu.cn

[c] A. Li, Z. Wang
Aeronautical Engineering Institute, Civil Aviation University of China, Tianjin 300300, Jinbei Road 2898, Dongli District, Tianjin, P.R. China

 Supporting information for this article is available on the WWW under <https://doi.org/10.1002/batt.202400446>

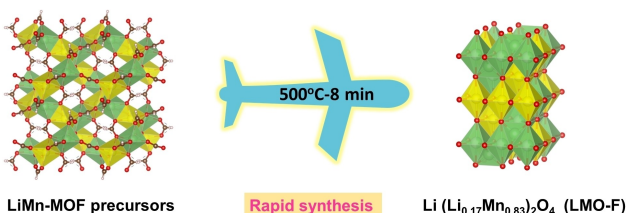


Figure 1. Low temperature and rapid synthesized Li-rich spinel cathodes from LiMn-MOF precursors.

LMO-F was systematically investigated by thermogravimetric analysis (TGA), and variable temperature X-ray diffraction (XRD). Notably, the LMO-F achieved good electrochemical performance with 100.4 mAh g^{-1} at 50 mA g^{-1} after 100 cycles, surpassing most previously reported LMO cathodes (Table S1).

Results and Discussion

2.1. Transformation of MOF Precursors to LMO

Aiming at the illustrations of the rapid synthesis mechanism and relationship between the MOF precursors and the corresponding Li-rich spinel materials, the composition and structural evolution during the pyrolysis process was systematically investigated.

For a better understanding, the structure of MOF precursor is briefly described below. The LiMn-MOF was synthesized by a self-assembly process using precursors of manganese nitrate tetrahydrate ($\text{Mn}(\text{NO}_3)_2 \cdot 4\text{H}_2\text{O}$), lithium hydroxide (LiOH) and formic acid (HCOOH). X-ray crystallographic analysis reveals that the LiMn-MOF crystallizes in the cubic structure in $P2_3$. Both of

cations are in distorted octahedral arrangements, each bonding to two crystallographically distinct oxygen anions (Figure 2a). The lattice planes of the LiMn-MOF was simulated using the Bravais–Friedel–Donnay–Harker (BFDH) method (Figure 2b). The XRD pattern of the as-synthesized LiMn-MOF is consistent with the simulated data, suggesting a successful synthesis of LiMn-MOF. (Figure 2c). Rietveld refinement analysis reveals that the calculated lattice parameters for LiMn-MOF are $a=b=c=8.7675 \text{ \AA}$, as illustrated in the Figure S1.

Theoretically, the process from decomposition of LiMn-MOF to formation of Li-rich spinel LMO are as follows: (1) Broken bond. According to the crystallographic data, the bond lengths of LiMn-MOF are given in Table S2 in the order of $\text{Li}-\text{O} \approx \text{Mn}-\text{O} > \text{C}-\text{O}$, indicating that the bond energies are in the order of $\text{Li}-\text{O} \approx \text{Mn}-\text{O} < \text{C}-\text{O}$. (2) Diffusion. After bond breaking, the diffusion of Li ions and Mn ions is mainly influenced by their concentration and radius, which are almost similar in the LiMn-MOF. (3) Nucleation. The ultra-small distance (3.190 \AA) and uniform distributions of Li and Mn ions in the LiMn-MOF would promote the phase transformation from MOF to transition metal oxides in a short time.

Experimentally, component evolution was monitored during the calcination process by TGA to probe the transformation process. TGA measurements were performed from 50 to 900°C with a heating rate of $10^\circ\text{C min}^{-1}$ in air (Figure 2d). The organic species were burned into CO_2 , leading to 68.5% weight loss according to the theoretical calculations, while the formation of metal oxide caused 18.5% weight gain upon the uptake of oxygen. The TGA measurement results are consistent with the theoretical values based on mass conservation of Mn. Besides, the structure and component evolution during the pyrolysis process were monitored by variable temperature XRD (Figure 2e). The diffraction peaks of the LiMn-MOF are well retained

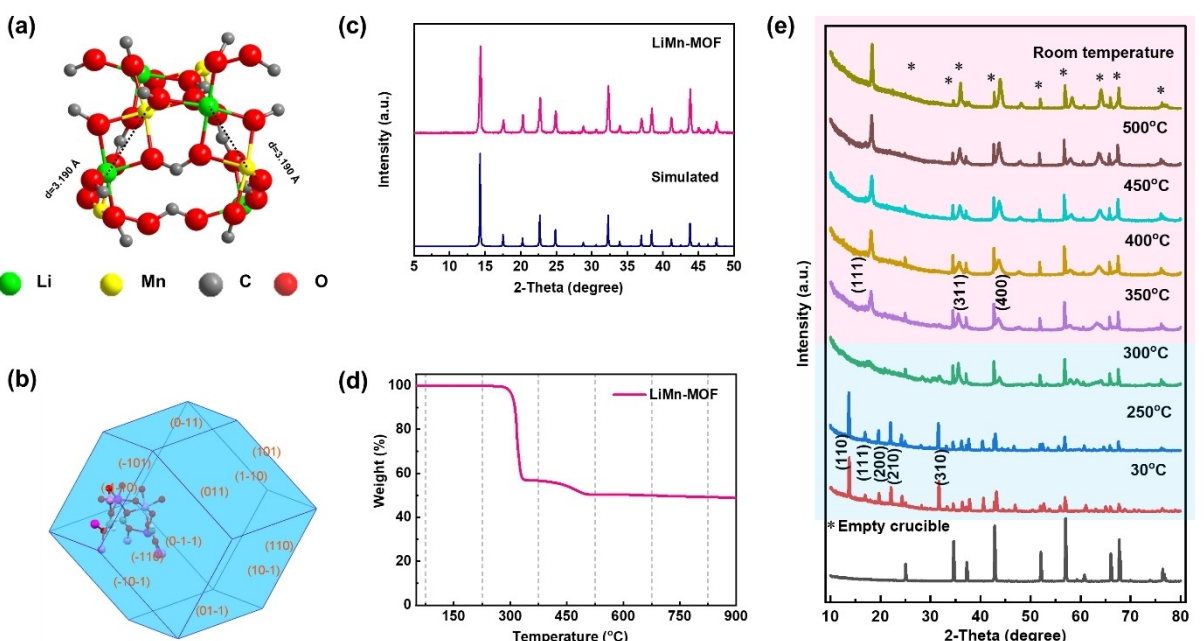


Figure 2. The LiMn-MOF of (a) Coordination environments, (b) Simulated crystal morphology, (c) XRD pattern, (d) TGA curve, (e) Variable temperature XRD patterns

until 250 °C. Interestingly, almost all of the diffraction peaks corresponding to the (110), (111), (200), (210), and (310) crystal planes of LiMn-MOF disappeared at 300 °C. These results are consistent with bond energies of LiMn-MOF ($\text{Li}-\text{O} \approx \text{Mn}-\text{O}$). From 350 °C, new peaks appeared at 18.8°, 36.6° and 44.5°, which can be indexed to the planes of (111), (311) and (400) of Li-rich spinel LMO, respectively. The variable temperature XRD measurement results show that Li-rich spinel can be facilely synthesized from the LiMn-MOF through thermal sintering. Based on TGA and variable temperature XRD results, the calcination temperatures of 450 °C and 500 °C were chosen and the calcination times were tried. Considering the crystallinity of the products, the reaction conditions at 500 °C for 8 min were chosen for rapid synthesis of $\text{Li}_{1+x}\text{Mn}_{2-x}\text{O}_4$ (Figure S2).

2.2. Synthesis and Properties of LMO-F and LMO-S

A low temperature and ultra-rapid synthesis method has been developed for the production of transition metal oxides, which involves sintering LiMn-MOF in a tube furnace preheated to 500 °C for 8 minutes in air, and the resulting product is denoted as LMO-F. As a control, transition metal oxide was also prepared using a long time sintering method (at 500 °C for 5 h with a heating rate of 2 °C min⁻¹ in air) from the same MOF precursor, denoted as LMO-S. Their spinel crystal structures were revealed by the XRD patterns, and they are in good agreement with Li-rich spinel $\text{Li}(\text{Li}_{0.17}\text{Mn}_{0.83})_2\text{O}_4$ (PDF#01-088-

0460) (Figure 3a). No impurities were detected, indicating the high phase purity of the product. XPS survey spectra of LMO show strong peaks of Mn 2p, Li 1s and O 1s (Figure S3). The high-resolution Mn 2p spectrum for LMO-F could be fitted at 642.6 eV and 654.1 eV, which correspond to the characteristic peaks of $\text{Mn}^{4+} 2p_{3/2}$ and $\text{Mn}^{4+} 2p_{1/2}$, respectively (Figure 3b). A similar XPS spectrum of Mn 2p was obtained for LMO-S. On the other hand, the high-resolution spectrum of Mn 3s for LMO-F can be deconvoluted into two peaks at 84.85 eV and 89.3 eV (Figure 3c). The average oxidation state of Mn V_{Mn} can be evaluated from the energy separation difference (ΔE_{3s}). The V_{Mn} of Mn in LMO-F was calculated to be 3.91, according to the linear relation: $V_{\text{Mn}} = 7.875 - 0.893\Delta E_{3s}$. The V_{Mn} of LMO-S, calculated by the same formula, is 3.95, which is very close to the value of 4.

The morphologies and microstructures of LMO-F and LMO-S were characterized by scanning electron microscopy (SEM) and transmission electron microscopy (TEM). The SEM images of them present similar morphologies, which is composed of nanosheets with irregular sizes (Figures 3d-g). Meanwhile, the TEM images of LMO-F and LMO-S in Figures 3h and j further identify the nanosheets structure. In addition, the HRTEM images indicate a clear lattice spacing of 4.7 Å (Figures 3i and k), which is in good agreement with the (111) planes of Li-rich spinel $\text{Li}(\text{Li}_{0.17}\text{Mn}_{0.83})_2\text{O}_4$. Apparently, well-crystallized $\text{Li}(\text{Li}_{0.17}\text{Mn}_{0.83})_2\text{O}_4$ can be produced by the fast synthesis process similar to the long time calcination process

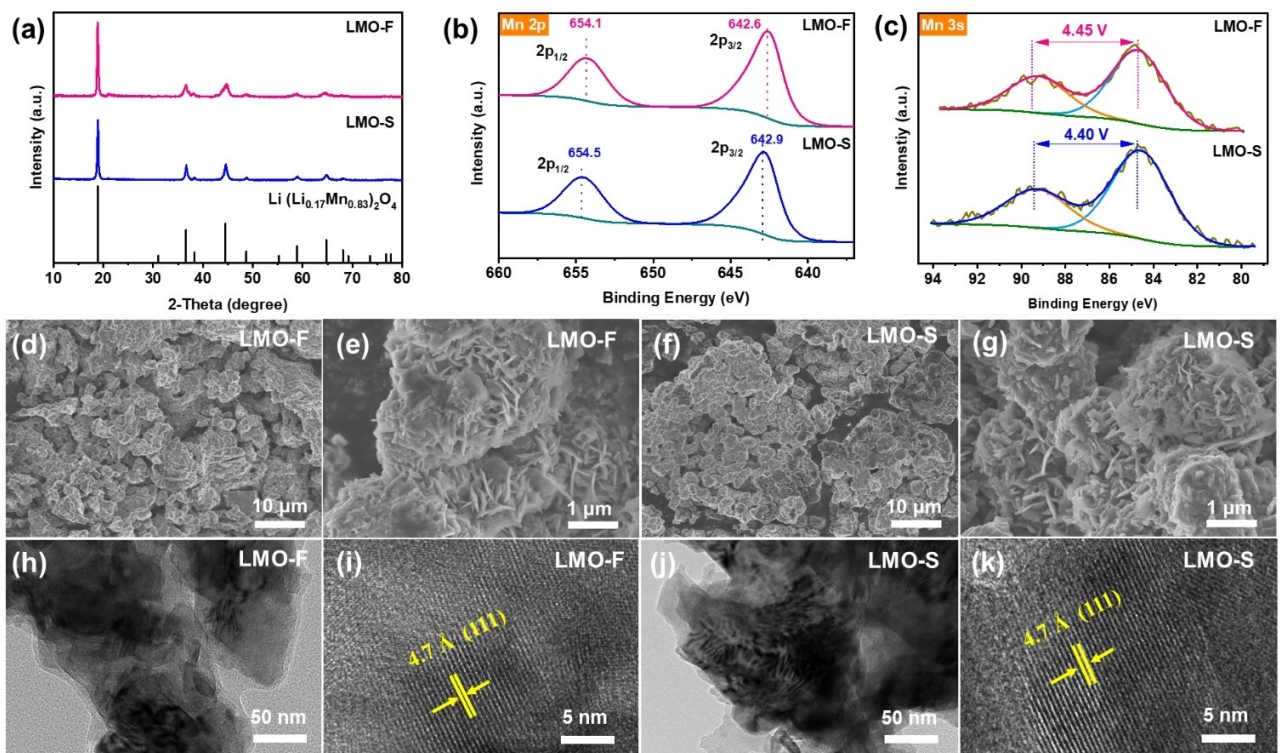


Figure 3. (a) XRD patterns of LMO-F and LMO-S, (b-c) Mn 2p and Mn 3s XPS spectra of LMO-F and LMO-S, (d-e) SEM images of LMO-F, (f-g) SEM images of LMO-S, (h-i) TEM images of LMO-F, (g-k) TEM images of LMO-S.

from the LiMn-MOF, demonstrating the effectiveness and superiority of MOF precursors for cathodes.

2.3. Electrochemical Characterization

On the basis of structural and component characterizations, the electrochemical performances of LMO-F and LMO-S were evaluated under the same test conditions. The cyclic voltammetry (CV) measurements were carried out at a scan rate of 0.1 mV s^{-1} in a voltage window of 1.8–3.6 V (vs. Li^+/Li). Similar CV curves were displayed for the LMO cathodes with redox couples at 2.8/3.0 V (Figures 4a and b), suggesting similar electrochemical behaviors. Compared with LMO-F, the cathodic peak of LMO-S cathode located at 2.2 V is more obvious. The electrochemical behaviors of LMO cathodes can be interpreted based on systematic investigations of Li^+ intercalation in the spinel phase $\text{Li}_{1+x}\text{Mn}_{2-x}\text{O}_4$.^[10] The observation of a plateau at 2.8 V is typical for the $\text{Li}_{1+x}\text{Mn}_{2-x}\text{O}_4$ spinel, in which Li^+ is intercalated into 16c octahedral sites corresponding to the composition range ($1 < 1+x \leq 2$).^[11] The origin of peak located at 2.2 V is unclear, and a similar phenomenon of defect Li-rich spinel cathodes ($\text{Li}_{1+x}\text{Mn}_{2-x}\text{O}_4$) also has been found in some

reported literatures.^[12] It has been proposed that the reaction about 2.2 V is due to particle size effects : Li^+ in 16c octahedral sites is concomitant with a cubic-to-tetragonal spinel transformation.^[13] The curves of CV almost overlap after the first scanning, suggesting that the LMO cathodes show the reversible electrochemical process and good stability during the discharge/charge process. Figures 4c and d show the charge/discharge curves of LMO-F and LMO-S at 20 mA g^{-1} within a cutoff voltage window of 1.8–3.6 V. For the first discharge process, a long voltage plateau at around 2.8 V corresponds to Li^+ ions insertion into the octahedral sites of spinel LMO cathodes, which is in accordance with the CV results.^[12c] The cycling performances of LMO-F and LMO-S are conducted at a current density of 50 mA g^{-1} (Figure 4e).The first discharge capacities of LMO-F and LMO-S are 111.9 and 120 mAh g^{-1} , respectively. For LMO-F, the capacity of 100.4 mAh g^{-1} and stable columbic efficiency of over 99% are obtained after 100 cycles. Although LMO-S cathode delivered a slightly higher initial capacity, similar cycling performance was obtained for LMO-F. LMO-F and LMO-S cathodes retained 90% and 93% of their initial capacity after 100 cycles at 50 mA g^{-1} , respectively. Moreover, the LMO-F delivers an initial discharge capacity of 81.9 mAh g^{-1} at 500 mA g^{-1} and retains 85% of its capacity after

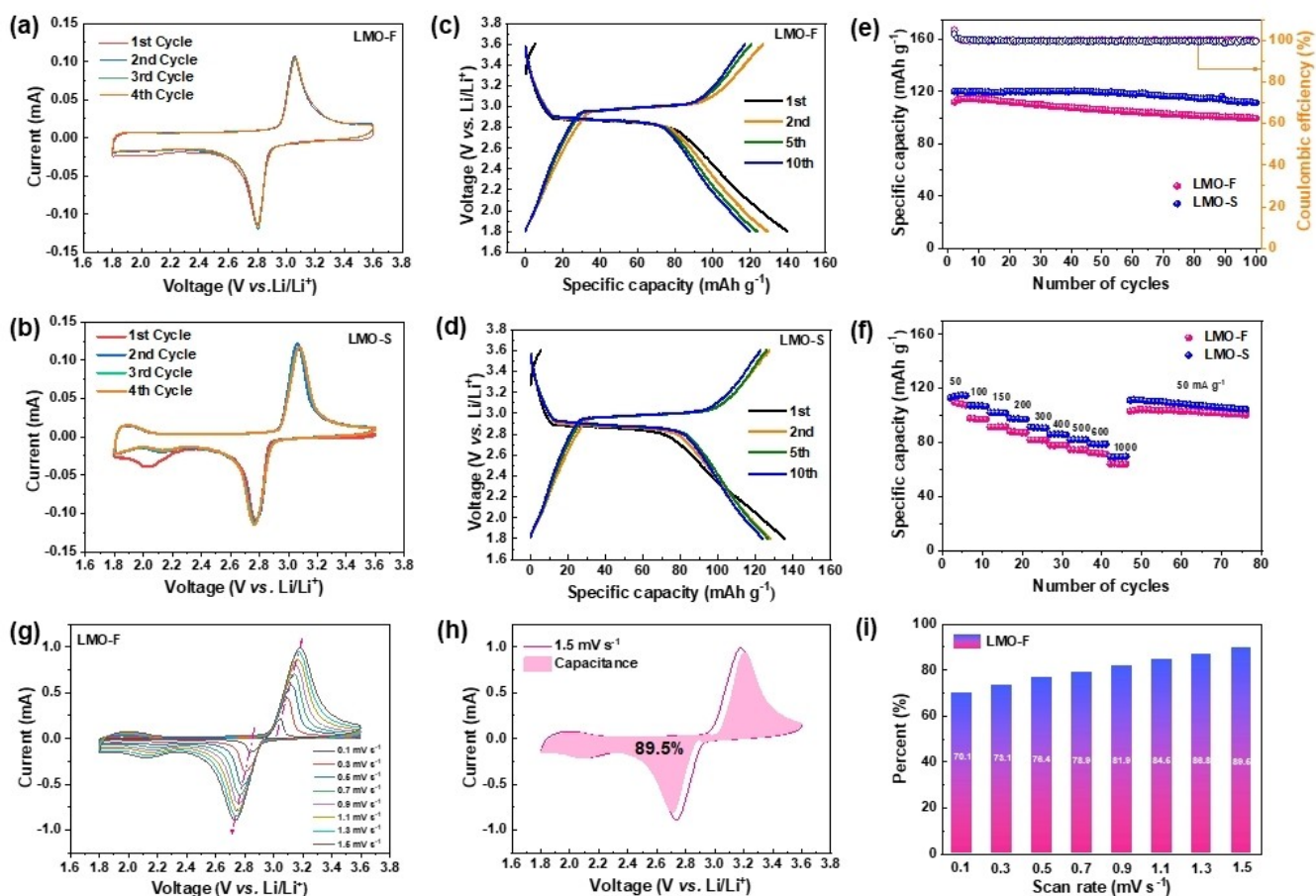


Figure 4. CV profiles of (a) LMO-F and (b) LMO-S at a scan rate of 0.1 mV s^{-1} . Galvanostatic charge–discharge profiles of (c) LMO-F and (d) LMO-S at the 1st, 2nd, 5th, and 10th cycles at 20 mA g^{-1} . (e) Cycling performance and coulombic efficiency of LMO-F and LMO-S at a current density of 50 mA g^{-1} . (f) Rate performance of LMO-F and LMO-S. Storage process characterization, (g) CV curves of the LMO-F cathode at different scan rates, (h) Capacitive contribution to the charge storage at 1.5 mV s^{-1} , and (i) Normalized capacitive-controlled capacities for LMO-F cathodes at different scan rates.

100 cycles (Figure S4). Excellent rate performance was obtained for both LMO–F and LMO–S (Figure 4f). When the current density increased from 50 to 1000 mA g⁻¹, LMO–F maintained a special capacity of 64 mAh g⁻¹, compared with 70 mAh g⁻¹ for LMO–S. After the current density recovers to 50 mA g⁻¹, the capacities of LMO–F and LMO–S cathodes restore to 103 mAh g⁻¹ and 111 mAh g⁻¹, respectively.

To further investigate the lithium storage behavior for the LMO cathodes, CV measurements at various sweep rates from 0.1–1.5 mV s⁻¹ were carried out (Figure 4g and S5). As shown in Figure S6 and S7, power law relationship ($i = av^b$) is used to analyze relationship between peak current (i) and scanning rate (v), where b -value determines the type of charge storage. In our work, the b -value of LMO–F and LMO–S are ~ 0.6 , indicating that the electrochemical process of them are combined behavior of diffusion and pseudocapacitive process.^[14] The capacity contributions from surface pseudo-capacitance and ion intercalation can be quantitatively calculated. According to the following equation: $i(V) = k_1v_1 + k_2v^{1/2}$, the charge storage should be divided into two parts: surface pseudocapacitive controlled (k_1v_1) and diffusion-controlled ($k_2v^{1/2}$) processes.^[15] Figure 4h and S8 show that capacitive contributions of LMO–F and LMO–S at 1.5 mV s⁻¹ were 89.5% and 88.9%, respectively. The surface capacitive-controlled capacities for LMO–F and LMO–S at different scan rates are summarized in Figure 4i and S9. LMO–F shows slightly higher diffusion-controlled capacities at various sweep rates. Besides, the electrochemical impedance spectroscopy (EIS) of LMO cathodes were investigated (Figure S10a). It is well known that the semicircle in the high frequency range is assigned to the charge transfer resistance (R_{ct}) on the surface and bulk of the electrode, and the sloping line in low-frequency region refers to the Warburg diffusion resistance in the Nyquist plot.^[16] The LMO–S possesses a smaller impedance and a more inclined line, indicating a relatively low electrode/electrolyte interfacial resistance and a smaller diffusion resistance of Li⁺ in the electrode compared with LMO–F. This phenomenon could be attributed to the better crystallinity of LMO–S, which allows easier access of Li⁺. The equivalent circuit used to fit the obtained impedance data is shown in the Figure S10b.

Conclusions

In this work, a low temperature and fast synthesis strategy is developed by directly calcining Li[Mn(HCOO)₃] for preparing Li-rich spinel Li(Li_{0.17}Mn_{0.83})₂O₄ cathode materials, thanks to the ultra-small distance (3.190 Å) and uniform distribution of Li and Mn ions in the LiMn-MOF. The fast phase transformation process was systematically investigated using multiple analysis techniques and theoretical simulations. The Li-rich spinel Li-(Li_{0.17}Mn_{0.83})₂O₄ cathode demonstrated excellent electrochemical performance with high reversibility and cycling stability, similar to the cathode produced by long-time calcination from the same precursor. Our findings prove that MOF is an ideal precursor for establishing a balance between the well-crystallized phase and stoichiometric chemistry of Li_{1+x}Mn_{2-x}O₄.

Experimental Section

Chemicals

All the reagents and solvents, including manganese nitrate tetrahydrate (Mn (NO₃)₂·4H₂O, Aladdin, 98%), lithium hydroxide (LiOH, Meryer, 98%) and formic acid (HCOOH, Meryer, 98%), methanol (CH₃OH, Tianjin Jiangtian Chemical Technology Co., Ltd, AR) and Dimethylformamide (DMF, Tianjin Jiangtian Chemical Technology Co., Ltd, AR) were commercially obtained and used without further purification.

Synthesis of LiMn(HCOO)₃

The LiMn(HCOO)₃ precursor was prepared according to a previous report with some modification.^[17] In this approach, Mn(NO₃)₂·4H₂O (1 mmol) and LiOH (5 mmol), and H₂CO₂ (1 mL) were added to a 25 mL autoclavable glass jar containing 10 mL DMF and heated to 140 °C. After heating at this temperature for 72 h, the jars were cooled back to room temperature slowly over a period of 12 h to encourage crystallization, then the crystals were obtained and washed with methanol and air-dried.

Synthesis of LMO-F

The LiMn(HCOO)₃ precursor was loaded in a porcelain boat and calcined into a tube furnace that was pre-heated to 500 °C for 8 min in air.

Synthesis of KMO-S

The LiMn(HCOO)₃ precursor was loaded in a porcelain boat and calcined into a tube furnace, then calcined at 500 °C for 5 h with a heating rate of 2 °C min⁻¹ in air.

Materials Characterization

Room temperature XRD patterns were recorded on a Rigaku MiniFlex 600 X-ray diffractometer at 40 kV and 15 mA with a Cu-target tube. Variable temperature XRD data were collected in air using a X-ray diffractometer (SmartLabs) equipped with Cu K α radiation ($\lambda = 1.5406 \text{ \AA}$). SEM (JEOL JSM-7500F), TEM and HRTEM (JEOL JEM F200) were used to investigate the morphologies and structures of samples. XPS was performed on a PHI5000 VersaProbe system. TGA was performed on a Rigaku TG-DTA 8121 analyzer at a rate of 10 °C min⁻¹ from 25 to 900 °C.

Electrochemical Tests

LMO–F or LMO–S was mixed with Ketjen black (KB) and polyvinylidenefluoride (PVDF) at a weight ratio of 7: 2: 1 and dispersed in N-methyl pyrrolidone to form a slurry, which was cast onto Cu foils (12 mm*0.9 μm). The electrodes were dried at 100 °C in vacuum for 12 h. The mass loading of active material was 1.5–2 mg cm⁻². Pure lithium foil (15.6 mm*0.5 mm) was used as counter electrode, and the separator was a polypropylene membrane (Celgard 2400, 18 mm*25 μm). The electrolyte consists of a solution of 1 M LiPF₆ in ethylene carbonate (EC)/dimethyl carbonate (DMC) (1:1 in volume). The CR2032 coin cells were assembled in an argon filled glovebox (H₂O and O₂ < 0.1 ppm). Constant current tests were conducted on LAND-CT2001 A battery testers. CV profiles were collected on a Solartron 1470 Electrochemical Interface. EIS was performed on a Princeton VersaSTAT4 electrochemical workstation

over a frequency range of 10^5 – 10^{-2} Hz with an AC amplitude of 5 mV.

Acknowledgements

This work was supported by the Fundamental Research Funds for the Central Universities (Grant No. XJ2021007101).

Conflict of Interests

The authors declare no conflict of interest.

Data Availability Statement

The data that support the findings of this study are available from the corresponding author upon reasonable request.

Keywords: Lithium-ion batteries • Li-rich spinel cathodes • Rapid synthesis • Metal – organic frameworks

- [1] a) M. Armand, J. M. Tarascon, *Nature* **2008**, *451*, 652; b) Z. Yang, J. Zhang, M. C. W. Kintner-Meyer, X. Lu, D. Choi, J. P. Lemmon, J. Liu, *Chem. Rev.* **2011**, *111*, 3577.
- [2] M. Kotal, S. Jakhar, S. Roy, H. K. Sharma, *J. Energy Storage* **2022**, *47*, 103534.

- [3] M. M. Thackeray, W. I. F. David, P. G. Bruce, J. B. Goodenough, *MRS Bull.* **1983**, *18*, 461.
- [4] a) R. Zhu, J. Wang, J. Li, *Chem. Res. Chin. Univ.* **2021**, *37*, 1031; b) Y. Liu, G. Liu, H. Xu, Y. Zheng, Y. Huang, S. Li, J. Li, *Chem. Commun.* **2019**, *55*, 8118; c) X. Zhang, S. Q. Liu, B. Y. Wang, G. Q. Wang, H. Z. Du, X. Y. Wang, H. D. Zhang, S. Zhao, L. Wang, H. J. Yu, *Sci. China Chem.* **2024**, *67*, 87.
- [5] M. Bianchini, E. Suard, L. Croguennec, C. Masquelier, *J. Phys. Chem. C* **2014**, *118*, 25947.
- [6] H. Park, Z. Guo, A. Manthiram, *Small* **2024**, *20*, 2303526.
- [7] A. Li, C. Li, P. Xiong, J. Zhang, D. Geng, Y. Xu, *Chem. Sci.* **2022**, *13*, 7575.
- [8] W. Zhu, A. Li, Z. Wang, J. Yang, Y. Xu, *Small* **2021**, *17*, 2006424.
- [9] X. Zhang, W. Zi, J. Zhou, L. Zhou, J. Zhang, X. Xuan, *Inorg. Chem.* **2023**, *62*, 9501.
- [10] T. Takada, H. Hayakawa, H. Enoki, E. Akiba, H. Slegr, I. Davidson, J. Murray, *J. Power Sources* **1999**, *81*–*82*, 505.
- [11] S. Ivanova, E. Zhecheva, D. Nihntanova, M. Mladenov, R. Stoyanova, *J. Alloys Compd.* **2013**, *561*, 252.
- [12] a) Y. Xia, T. Sakai, C. Wang, T. Fujieda, K. Tatsumi, K. Takahashi, A. Mori, M. Yoshio, *J. Electrochem.* **2001**, *148*, A112; b) R. Alcántara, M. Jaraba, P. Lavela, J. L. Tirado, E. Zhecheva, R. K. J. C. O. M. Stoyanova, *Chem. Mater.* **2004**, *16*, 1573; c) W. Fu, T. Lei, B. Cao, X. Shi, Q. Zhang, Z. Ding, L. Chen, J. Wu, *J. Power Sources* **2024**, *618*, 235144.
- [13] M. M. Thackeray, A. de Kock, M. H. Rossouw, D. Liles, R. Bittihn, D. Hoge, *J. Electrochem.* **1992**, *139*, 363.
- [14] V. Augustyn, J. Come, M. A. Lowe, J. W. Kim, P.-L. Taberna, S. H. Tolbert, H. D. Abrúñia, P. Simon, B. Dunn, *Nat. Mater.* **2013**, *12*, 518.
- [15] J. Wang, J. Polleux, J. Lim, B. Dunn, *J. Phys. Chem. C* **2007**, *111*, 14925.
- [16] S. Wang, J. Zhang, O. Gharbi, V. Vivier, M. Gao, M. E. Orazem, *Nat Rev Methods Primers* **2021**, *1*, 41.
- [17] J. C. Aston, P. J. Saines, *Z Anorg Allg. Chem.* **2017**, *643*, 287.

Manuscript received: June 30, 2024

Revised manuscript received: October 14, 2024

Accepted manuscript online: October 14, 2024

Version of record online: November 9, 2024